

Photoinduced intermolecular electron transfer reaction between N,N dimethylaniline and anthracene in acetonitrile solution: A theoretical study

Koji Ando

Citation: *The Journal of Chemical Physics* **101**, 2850 (1994); doi: 10.1063/1.467599

View online: <http://dx.doi.org/10.1063/1.467599>

View Table of Contents: <http://scitation.aip.org/content/aip/journal/jcp/101/4?ver=pdfcov>

Published by the [AIP Publishing](#)

Articles you may be interested in

[Photoinduced electron transfer reaction in polymer-surfactant aggregates: Photoinduced electron transfer between N , N -dimethylaniline and 7-amino coumarin dyes](#)

J. Chem. Phys. **128**, 204510 (2008); 10.1063/1.2928812

[A femtosecond study of photoinduced electron transfer from dimethylaniline to coumarin dyes in a cetyltrimethylammonium bromide micelle](#)

J. Chem. Phys. **125**, 054509 (2006); 10.1063/1.2220570

[Computer simulation studies of electron transfer parameters for cyanoanthracene/N,N-dimethylaniline solutions](#)

J. Chem. Phys. **118**, 4149 (2003); 10.1063/1.1541617

[Time-resolved Raman study on the photoinduced intermolecular electron-transfer reaction of biphenyl in alcohols](#)

J. Chem. Phys. **110**, 9179 (1999); 10.1063/1.478840

[A theoretical study of outersphere electron transfer reactions in electrolyte solutions](#)

J. Chem. Phys. **110**, 1569 (1999); 10.1063/1.477815



Photoinduced intermolecular electron transfer reaction between *N,N*-dimethylaniline and anthracene in acetonitrile solution: A theoretical study

Koji Ando^{a),b)}

Department of Chemistry, Faculty of Science, Kyoto University, Kitashirakawa, Sakyo-ku, Kyoto 606, Japan

(Received 30 November 1993; accepted 3 May 1994)

The photoinduced intermolecular electron transfer (ET) reaction between *N,N*-dimethylaniline and excited state anthracene in acetonitrile solution is studied theoretically. A solvation coordinate s which represents stochastic one-dimensional dynamics of the solution phase reaction is defined and a Hamiltonian in terms of s and perpendicular bath modes is derived from the spin-boson Hamiltonian. This has an advantage that the dynamics of the transferring electron is influenced by the bath only through coupling with the coordinate s . Intra- and intermolecular potentials are constructed by using *ab initio* molecular orbital methods, and a series of molecular dynamics simulation analysis is performed. Mean force potentials as a function of the donor-acceptor distance R are computed and the bimolecular encounter dynamics is investigated. Diabatic free energy curves for the coordinate s are computed and shown to be well approximated by parabolas, indicating that the dielectric saturation effect is negligible. The dependence of the free energy relationships on R is examined. It is shown that the present system corresponds to the increasing region of the rate constant, in contrast with the conventional picture. The electronic coupling of the ET is evaluated by the method of corresponding orbitals. The R dependence of the ET rate is evaluated and the reaction adiabaticity and mechanism are discussed. Dynamical solvent effects are taken into consideration in terms of the generalized Langevin equation formalism.

I. INTRODUCTION

Photoinduced electron transfer (ET) reactions in polar solvents are among the most important elementary processes in organic photochemistry.¹⁻¹⁵ Considerable attention has been paid to the reaction mechanism because it is regarded as a prototype of nonadiabatic electronic transition processes in condensed phase.¹⁶⁻²⁸ In ET reactions in polar solvents, the electrostatic coupling of the solvent polarization to the reaction can be quite strong that the dominant contribution to the activation energy may come from the solvent reorganization. The outer-sphere ET has been usually described by the nonadiabatic regime of electronic transition because the electronic coupling between the initial and the final electronic states is considered to be small. Early theories developed by Marcus and others have considered the semiclassical nonadiabatic regime.¹¹⁻¹⁵ An important prediction is the existence of the "inverted region." Marcus predicted that the activation energy ΔG^\ddagger is given by¹¹

$$\Delta G^\ddagger = (\Delta G^0 + \lambda)^2 / 4\lambda, \quad (1.1)$$

where ΔG^0 and λ are the standard free energy and the reorganization energy of the reaction. This indicates that the ET rate increases with decreasing ΔG^0 at small $|\Delta G^0|$ region to a maximum at $\Delta G^0 = -\lambda$, and then decreases as ΔG^0 becomes more negative (more exothermic). The region of decline is termed the inverted region.

Rehm and Weller pointed out the discrepancy between the theory and the experiment for the first time.²⁹ They measured rate constants of photoinduced charge-separation (CS) reactions as a function of ΔG^0 by varying the aromatic fluorescer-quencher pair in acetonitrile solution. In contrast to the theoretical prediction, the observed reaction rates are almost constant at a highly exothermic region and the inverted behavior is not seen down to $\Delta G^0 \sim -2.5$ eV. Mataga *et al.* experimentally showed that the electronic excited state does not contribute for the range of ΔG^0 down to -1.63 eV.³⁰ Miller *et al.* carried out a series of experiments for reactions between chemically linked redox centers that are unaffected by diffusion, and suggested the existence of the inverted effect.³¹ The quantum-mechanical perturbation theories show that the quantum correction predicts a smaller but still finite inversion.³² The contributions of the vibronic channels³³ and the dielectric saturation effects³⁴ have also been examined.

Theoretical calculations based on realistic molecular models of specific systems are expected to make a significant contribution to the problem. Although previous works on simple model ET reactions³⁵⁻³⁸ have shown the usefulness of the simulation study for understanding the ET mechanism, the problem of the photoinduced ET or the fluorescence quenching process in acetonitrile solution has not been addressed. In this work, we carry out a theoretical analysis on the photoinduced intermolecular ET reaction between *N,N*-dimethylaniline (DMA) and excited state anthracene in acetonitrile solution. The experimental energy gap ΔG^0 of this reaction is reported to be -0.54 eV, which corresponds to the region near the inversion according to the dielectric continuum model.^{29,30,33} In order to examine the free energy

^{a)}Japan Society for the Promotion of Science Fellow (April 1991–March 1993).

^{b)}Present address: Department of Chemistry and Biochemistry, University of Colorado, Boulder, Colorado 80309-0215.

relationships on the basis of precise molecular models, intra- and intermolecular potential energy functions are developed by using *ab initio* molecular orbital (MO) methods, and a series of molecular dynamics (MD) simulation analysis is performed. Considering the distribution of the donor-acceptor distance R should play an important role in the bimolecular reaction in solution, the mean force potential, and the diffusion behavior of R are examined. Free energy curves along the solvation coordinate are also constructed. We focus on their dependence on R . The solvation dynamics is analyzed and the dynamical quantities such as the frequency components of the reaction coordinate vector and the time-dependent friction kernel are deduced from the MD analysis.

In Sec. II, our theoretical model is summarized. The definition of the solvation coordinate s that extracts stochastic one-dimensional dynamics from the complicated solution phase reaction is given, and a Hamiltonian in terms of s and perpendicular bath modes is derived. Intra- and intermolecular potential energy functions are developed in Sec. III, with the use of the electron distribution of anthracene computed by *ab initio* MO methods. A series of MD simulation analysis is described in Sec. IV. Section V is devoted to a discussion on the ET mechanism. The electronic coupling of the reaction is computed in terms of charge-localized diabatic states by using the method of corresponding orbitals. The ET rates are evaluated as a function of the donor-acceptor distance R , and the nuclear tunneling effects, the reaction adiabaticity, and the solvent friction effects are discussed. Concluding remarks are given in Sec. VI.

II. THEORETICAL MODEL

Intermolecular ET in solution may occur over a range of the donor-acceptor distance R . To take account for this, we consider the diffusion process of R and the solvent driven ET as a function of R . Bimolecular ET in solution is then modeled by the following diffusion-reaction equation:

$$\frac{\partial}{\partial t} P(R, t) = [L_R - k(R)] P(R, t), \quad (2.1)$$

where $P(R, t)$ and $k(R)$ are the probability distribution function and the ET rate at R , respectively. L_R is a Smoluchowski-type linear operator of the form

$$L_R = \frac{D_{\text{DA}}}{R^2} \frac{\partial}{\partial R} R^2 \left(\frac{\partial}{\partial R} + \frac{1}{k_B T} \frac{\partial F(R)}{\partial R} \right), \quad (2.2)$$

in which D_{DA} and $F(R)$ denote the diffusion constant and the mean force potential for R . This model would be adequate when the kinematic time scale of the solvent fluctuation is shorter than that of the R diffusion, which is the case for the system considered here. Specifically, we take the DMA-anthracene center-of-mass (c.m.) distance for R .

To evaluate the ET rate constant $k(R)$, we consider a harmonic bath model coupled to a two-state system, which is discussed to be a reasonable approximation in Sec. IV. We employ the spin-boson Hamiltonian of the form²²⁻²⁷

$$H = |H'_{XI}(R)| \sigma_x - \frac{\Delta G^0(R)}{2} \sigma_z + H_B(\mathbf{p}, \mathbf{x}; R) + V(\mathbf{x}; R) \sigma_z, \quad (2.3a)$$

where σ_x and σ_z are the Pauli spin matrices with $\sigma_z = +1$ and -1 corresponding to the excited pair (XP) and the ion pair (IP) diabatic states, respectively. H'_{XI} denotes the electronic coupling between the two states (see Sec. V A). H_B and V are the bath Hamiltonian and the coupling between the electronic and the bath degrees of freedom expressed by

$$H_B(\mathbf{p}, \mathbf{x}; R) = \sum_i \left(\frac{p_i^2}{2} + \frac{\omega_i(R)^2}{2} x_i^2 \right), \quad (2.3b)$$

$$V(\mathbf{x}; R) = \sum_i c_i(R) x_i, \quad (2.3c)$$

where (x_i, p_i) denote the mass-scaled bath coordinate and its conjugate momentum, and ω_i and c_i are the frequency and the coupling strength for the i th mode. The quantities in the Hamiltonian depend parametrically on R in the model.

We define the solvation coordinate by the potential energy difference

$$s = f(\mathbf{x}; R) = W_{\text{XP}}(\mathbf{x}; R) - W_{\text{IP}}(\mathbf{x}; R), \quad (2.4)$$

where W_{XP} and W_{IP} are potential energies of the two diabatic states. This choice would be adequate with respect to a surface hopping picture of the nonadiabatic ET since the potential energies of the two states always coincide at $s=0$.³⁵⁻⁴¹ The minimum energy point \mathbf{x}^\ddagger of the crossing seam $s=0$ could be considered as the transition state of the reaction, which is given by

$$\mathbf{x}_i^\ddagger = \frac{c_i / \omega_i^2}{(\sum_j c_j^2 / \omega_j^2)} \frac{\Delta G^0}{2} = \frac{c_i}{\omega_i^2} \frac{\Delta G^0}{\lambda}, \quad (2.5)$$

where (and hereafter) the parametrical dependence on R is abbreviated.

The energy difference coordinate like Eq. (2.4) has been used in many simulation studies, and shown to be a useful choice for a microscopic representation of the many-dimensional solvent motion.^{35-38,40,41} In particular, it is directly related to the nonadiabatic Golden Rule formula of the thermal rate constant.^{35,66} A mechanical significance of the coordinate has been shown by Kato *et al.* for gas-phase molecular reactions,³⁹ and by Ando and Kato for a solution phase harmonic bath model.⁴¹ Here we show an alternative way based on a simpler idea, and derive a transformed Hamiltonian represented by the coordinate s and perpendicular bath modes.

First, we see the coordinate s defined by Eq. (2.4) is linear in \mathbf{x} or the displacement vector $\tilde{\mathbf{x}} = \mathbf{x} - \mathbf{x}^\ddagger$, i.e.,

$$s = W_{\text{XP}}(\mathbf{x}) - W_{\text{IP}}(\mathbf{x}) = 2 \sum_i c_i x_i - \Delta G^0 = 2 \sum_i c_i (x_i - x_i^\ddagger). \quad (2.6)$$

This implies the significance of a unit vector $\tilde{\mathbf{s}}$ composed of the potential coupling coefficients c_i ,

$$\tilde{s}_i = c_i / \left(\sum_j c_j^2 \right)^{1/2}. \quad (2.7)$$

The energy difference coordinate s is now proportional to $\tilde{s} = \tilde{\mathbf{s}} \cdot \tilde{\mathbf{x}}$, a scalar projection of $\tilde{\mathbf{x}}$ onto $\tilde{\mathbf{s}}$, i.e.,

$$s = 2 \left(\sum_i c_i^2 \right)^{1/2} \tilde{s}. \quad (2.8)$$

It is shown below [Eq. (2.10)] that the factor $2(\sum_i c_i^2)^{1/2}$ is related to the effective mass of s . The vector $\tilde{\mathbf{s}}$ is the same as the "reaction coordinate vector" defined by the steepest descent path passing through \mathbf{x}^\ddagger in the mass-weighted Cartesian coordinate space.^{39,41} It is noted, however, that the coordinate s is different from the so-called reaction path coordinate: a close connection is found only at \mathbf{x}^\ddagger .

To derive a Hamiltonian for s and the normal bath coordinates perpendicular to it, it is convenient to employ a projection operator $\hat{\mathbf{P}}$ with the element

$$\hat{P}_{ij} = c_i c_j / \sum_k c_k^2, \quad (2.9)$$

and the matrix partitioning technique with $\hat{\mathbf{Q}} = \mathbf{I} - \hat{\mathbf{P}}$. After some straightforward manipulation, we obtain

$$H = \tilde{H}_S + \tilde{H}_B + \tilde{V} + (\Delta G^0)^2 / 4\lambda, \quad (2.10a)$$

$$\tilde{H}_S = |H'_{X1}| \sigma_x + \frac{p_s^2}{2\mu} + \frac{\mu \tilde{\omega}^2}{2} s^2 + \frac{1}{2} \left(\sigma_z + \frac{\Delta G^0}{\lambda} \right) s, \quad (2.10b)$$

$$\tilde{H}_B = \sum_i \left(\frac{\tilde{p}_i^2}{2} + \frac{\tilde{\omega}_{Q,i}^2}{2} \tilde{y}_i^2 \right), \quad (2.10c)$$

$$\tilde{V} = \left(\sum_i \tilde{\omega}_{PQ,i}^2 \tilde{y}_i \right) \mu^{1/2} s. \quad (2.10d)$$

\tilde{H}_S shows that the dynamics of the coordinate s is characterized by the frequency $\tilde{\omega} \equiv \sum_i \omega_i^2 \tilde{s}_i^2$ and the effective mass $\mu \equiv (4 \sum_i c_i^2)^{-1}$. Frequencies of the bath modes $\tilde{\omega}_{Q,i}$ are obtained by diagonalizing the matrix $\omega_{QQ}^2 \equiv \hat{\mathbf{Q}} \omega^2 \hat{\mathbf{Q}}$, whose elements are expressed as

$$\omega_{QQ,ij}^2 = \omega_i^2 \delta_{ij} + (\tilde{\omega}^2 - \omega_i^2 - \omega_j^2) \tilde{s}_i \tilde{s}_j. \quad (2.11)$$

\tilde{V} represents bilinear coupling between s and the bath modes \tilde{y}_i with the coupling strength of $\tilde{\omega}_{PQ,i}^2$ which is obtained by unitary transforming the column vector $\omega_{PQ,i}^2 = (\omega_i^2 - \tilde{\omega}^2) \tilde{s}_i$ by using the eigenvectors of ω_{QQ}^2 corresponding to the non-zero eigenvalues (ω_{QQ}^2 has a zero eigenvalue corresponding to the direction of $\tilde{\mathbf{s}}$).

The Hamiltonian of the form [Eq. (2.10)] has several advantageous features. Above all, the dynamics of the transferring electron is influenced by the bath only through the coupling with the one-dimensional coordinate s in this representation. Thus, we can examine the reaction dynamics by averaging out the bath influences and focusing on the stochastic dynamics of s . A similar kind of transformation has been mentioned in a rather heuristic way by Garg *et al.*²³

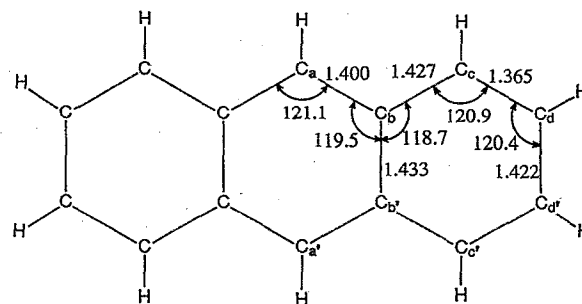


FIG. 1. Geometrical parameters of anthracene $C_{14}H_{10}$. Bond distances are in Å and angles in deg. All the CH bond distances are 1.08 Å.

Classical dynamics of the solvation coordinate is described by the generalized Langevin equation of the form^{10,41,67}

$$\ddot{s} + \Omega^2 s + \int_0^t \zeta(\tau) \dot{s}(t-\tau) d\tau + \mu^{-1} \bar{g} + \zeta(t) s(0) = \mu^{-1/2} R(t), \quad (2.12)$$

where $\Omega \equiv [\tilde{\omega}^2 - \zeta(0)]^{1/2}$ denotes the effective frequency for the harmonic free energy curve along s and $\bar{g} = \sum_i (c_i \sigma_z + \omega_i^2 x_i^\ddagger) \tilde{s}_i = (\sigma_z + \Delta G^0 / \lambda) / 2$. The time-dependent friction kernel $\zeta(t)$ is given by

$$\zeta(t) = \sum_i \frac{(\tilde{\omega}_{PQ,i}^2)^2}{\tilde{\omega}_{Q,i}^2} \cos(\tilde{\omega}_{Q,i} t), \quad (2.13)$$

which is related to the random force $R(t)$ by the second fluctuation-dissipation theorem $\langle R(0)R(t) \rangle = k_B T \zeta(t)$. We can also compute the spectral density of the bath modes given by

$$J_b(\omega) = \frac{\pi}{2} \sum_i \frac{(\tilde{\omega}_{PQ,i}^2)^2}{\tilde{\omega}_{Q,i}^2} \delta(\omega - \tilde{\omega}_{Q,i}), \quad (2.14)$$

which is useful for quantum-mechanical treatments. Note that $J_b(\omega)$ represents the influence of the bath modes \tilde{y}_i on the "solvation coordinate+transferring electron" subsystem in the transformed Hamiltonian [Eq. (2.10)], and is different from the usually considered spectral density [given in Eq. (5.4c) below] associated with the original Hamiltonian [Eq. (2.3)].

III. POTENTIAL ENERGY FUNCTIONS

Potential energy functions of DMA and anthracene in acetonitrile solution are determined by *ab initio* MO calculations. The potential functions for DMA and DMA⁺ are taken from Ref. 41. We present here only the potential functions of anthracene.

A. Electronic states of anthracene

The electronic wave functions of the ground, excited, and anion states of anthracene are calculated with the spin-restricted Hartree-Fock (HF) approximation.⁴² For the excited and the anion states, the spin-restricted open-shell HF

TABLE I. Effective point charges on anthracene.

	Ground	Excited	Anion
C _a	-0.1950	-0.2048	-0.4524
C _b	0.0839	0.1307	0.1584
C _c	-0.2237	-0.2702	-0.2742
C _d	-0.1317	-0.1526	-0.2245
H	0.1476	0.1578	0.1266

wave functions are employed.⁴³ We assume that the excited state of anthracene is described by the B_{2u} ($\pi-\pi^*$) configuration.⁴⁴ The experimental geometry of C₁₄D₁₀ is used⁴⁵ except that the CH bond length is set to be 1.08 Å (Fig. 1). The basis set used is the 6-31G set⁴⁶ and the number of basis functions is 146. As expected, the HF approximation does not give quantitative values of both the excitation energy and the electron affinity, while the electron distribution would be accurate enough for the current purpose. The excitation energy and the electron affinity are computed to be 5.0 and -1.2 eV, respectively, whereas the experimental values are reported to be 3.4 and +0.5 eV.^{47,48} We use these experimental values as a correction in constructing the potential energy functions for the simulation analysis.

B. Intermolecular potential functions

With the use of the electron distribution from the MOs, the intermolecular pair potential function is developed. It is assumed to be described by a sum of electrostatic and exchange-exclusion parts. These are implemented by the effective point charge model and the Gordon–Kim model,^{40,49} respectively. The potential functions are expressed in a form,

$$V^{\text{int}} = \sum_a \sum_b \left[\frac{q_a q_b}{r_{ab}} + 4\epsilon_{ab} \left\{ \left(\frac{\sigma_{ab}}{r_{ab}} \right)^{12} - \left(\frac{\sigma_{ab}}{r_{ab}} \right)^6 \right\} \right], \quad (3.1)$$

where the subscripts a and b denote atoms or extended atoms of the interacting molecules. The effective charges on the atom sites of anthracene are determined so as to reproduce the electrostatic potential at ~500 points around the molecule. All the H atoms are assumed to have a common value of the effective charge. The results are shown in Table I. The negative charge of the anion mainly distributes around the C_a and C_{a'} atoms, which is consistent with the MO coefficients of the lowest unoccupied MO (LUMO) of anthracene. The exchange-exclusion potential is computed by the Gordon–Kim model and fitted to the 12-6 Lennard-Jones function. First, the pair interaction energies between the C atoms or CH moieties in anthracene and H₂O molecule are calculated. Then, the length and energy parameters (σ and ϵ) are determined by using the geometric-mean combining rules. We use H₂O as the counterpart molecule because it is modeled as an extended atom and therefore is convenient for the procedure, which assumes the transferability of the parameters. Least-squares fitting is carried out under a condition that all the CH extended atoms have common parameters. We found that both σ and ϵ resulted in almost the same values among the three (ground, excited, and anion) elec-

TABLE II. Lennard-Jones parameters for anthracene.

	σ^a	ϵ^b
C(sp^2)	3.761 (3.750) ^c	0.0135 (0.105)
CH(arom)	3.913 (3.750)	0.0142 (0.110)

^aGiven in Å.

^bGiven in kcal/mol.

^cThe values in parentheses are from Ref. 50.

tronic states. The difference of the interaction potential among the states is thus represented by the difference in the electrostatic part.

The resultant parameters are listed in Table II. Corresponding ones from the optimized functions for liquid simulations (OPLS) model by Jorgensen *et al.*⁵⁰ are included for comparison, although the description of the electrostatic part is different, i.e., the charge parameters for C(sp^2) and CH(arom) are set to be zero in the OPLS model. The intra- and intermolecular potential functions for DMA and DMA⁺ are taken from Ref. 41. For the solvent acetonitrile, the parameters developed by Jorgensen and Briggs⁵¹ are used: $q_{\text{Me}}=0.15e$, $q_{\text{C}}=0.28e$, $q_{\text{N}}=-0.43e$, $\sigma_{\text{MeMe}}=3.775$ Å, $\sigma_{\text{CC}}=3.650$ Å, $\sigma_{\text{NN}}=3.200$ Å, $\epsilon_{\text{MeMe}}=0.207$ kcal/mol, $\epsilon_{\text{CC}}=0.150$ kcal/mol, and $\epsilon_{\text{NN}}=0.170$ kcal/mol.

IV. MOLECULAR DYNAMICS CALCULATION

A. Method

The simulation analysis of the solution phase reaction is carried out by classical MD trajectory methods. For the solute DMA, two large amplitude internal modes—the wagging motion of the dimethylamino group (θ) and the torsional motion around the NC bond (τ)—are treated explicitly (Fig. 2). Details of the method to compute the trajectory of DMA in terms of the internal coordinates (θ, τ) have been presented.⁴¹ In brief, the motion of the DMA molecule is described by using the G -matrix formula, and the Coriolis coupling between the θ, τ -vibrational motions and the rotational motion of the molecule is eliminated by defining the body-fixed rotational axes as functions of θ and τ . The solute anthracene and the solvent acetonitrile are treated as rigid bodies. Quaternion parameters^{52,53} are utilized to describe the rotational motion of all the species. Integration of the equations of motion is performed by the Gear predictor–corrector method initiated by the fourth-order Runge–Kutta method. The five- and four-values Gear algorithms⁵⁴ are applied for the first- and second-order equations of motion,

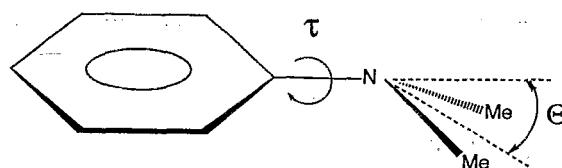


FIG. 2. Large amplitude intramolecular vibrational modes of DMA; wagging motion of the dimethylamino group (θ) and torsional motion around the NC bond (τ).

respectively. The periodic boundary condition is applied. In each cubic cell, a pair of DMA and anthracene molecules is surrounded by 500 acetonitrile molecules. The mass density of the system is assumed to be the same as that of liquid acetonitrile, 0.765 g/cm^3 , which has been obtained in Ref. 51 by the constant pressure Monte Carlo simulation using the same potential functions of acetonitrile as used here. The simulation box length is then 35.6 \AA . The potential tapering method with a fifth-order tapering function^{41,55} is applied to all the interaction potentials: the pair interaction is smoothly damped in the region $0.45L < R_{\text{c.m.}} < 0.5L$, where $R_{\text{c.m.}}$ and L denote the distance between c.m. of two interacting molecules and the simulation box length, respectively. A constant correction value is introduced to the potential function so that the ΔG^0 at $R=12 \text{ \AA}$ reproduces the experimental value. Equilibrium MD calculations are carried out after careful (several 10 ps of) cooling and equilibration runs. Good energy conservation ($\Delta E < 0.6 \text{ kcal/mol}$) is achieved with the use of a time step of 0.5 fs. No temperature controlling algorithm is used in all the equilibrium and nonequilibrium simulations. After the equilibration, the kinetic temperature of the system was found to be kept around $298 \pm 3 \text{ K}$ in the equilibrium simulations.

B. Diffusion of donor and acceptor molecules

As the intermolecular ET in solution may occur over a range of R , its distribution must be taken into consideration. When the ET rate at some encounter distance is sufficiently large, the reaction rate observed by the steady-state measurements may be masked by diffusion.^{31,32} The essential features of the encounter dynamics of the donor-acceptor pair are reflected in the mean force (mf) potential and the diffusion coefficient for R . The mf potential as a function of R is computed by using the umbrella sampling method. The bias potential employed is of the form

$$U(R) = a(R - R_0)^2. \quad (4.1)$$

The parameters used are $(a, R_0) = (1.0, 2.0), (1.9, 2.0), (9.7, 2.0), (1.9, 3.0), (1.0, 4.0), (1.0, 6.0)$, and $(1.9, 10.0)$, where a and R_0 are given in $\times 10^{-2} \text{ eV/\AA}^2$ and \AA , respectively. All the sampling runs with the bias potential are carried out with the simulation time of 12.5 ps. The mf potential curves $F(R)$ are computed by

$$F(R) - F(R)_{\text{ref}} = -k_B T \ln[P(R)/P(R)_{\text{ref}}] - U(R) + C, \quad (4.2)$$

where $P(R)$ denotes the probability density for R . The reference potential $F(R)_{\text{ref}}$ is computed from simulation runs without the bias potential starting at $R=5$ and 7 \AA with the simulation time of 25 ps for each. The matching constant C is given by

$$C = -k_B T \ln\langle \exp(-U/k_B T) \rangle_{\text{ref}}, \quad (4.3a)$$

$$= +k_B T \ln\langle \exp(+U/k_B T) \rangle_{\text{bias}}. \quad (4.3b)$$

In practice, we use the average value of C 's computed from Eqs. (4.3a) and (4.3b).

Figure 3 shows the resultant mf potential curves for XP and IP states. $F(R)$ may be expressed as¹⁰

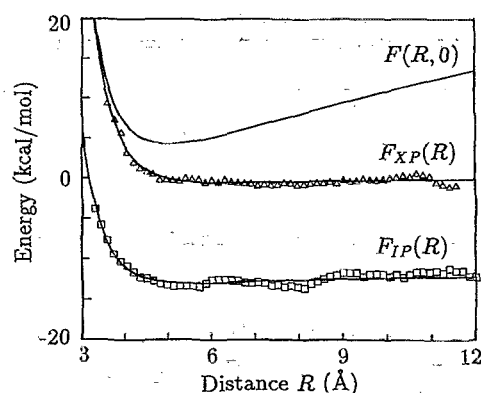


FIG. 3. Mean force potential curves along the DMA-anthracene center of mass distance R in acetonitrile solution. $F_{\text{XP}}(R)$ and $F_{\text{IP}}(R)$ are for the excited and ion pair states, respectively. The symbols Δ and \square are simulation results and solid curves are fitted ones. $F(R,0)$ represents the diabatic potential crossing seam (see Sec. IV C).

$$F(R) = W^{\text{DA}}(R) + \delta F(R), \quad (4.4)$$

where $W^{\text{DA}}(R)$ and $\delta F(R)$ denote the direct interaction between the donor and the acceptor molecules and the indirect effective potential due to the existence of the solvent, respectively. $W_{\text{XP}}^{\text{DA}}(R)$ and $W_{\text{IP}}^{\text{DA}}(R)$ are displayed in Fig. 4. They are averaged over the orientational distribution of the donor-acceptor pair as they are sampled in the simulation.

As seen in Fig. 3, $F_{\text{XP}}(R)$ exhibits a flat curve at the $R > 5 \text{ \AA}$ region. $F_{\text{IP}}(R)$ is also a flat one, which is noteworthy since $W_{\text{IP}}^{\text{DA}}(R)$ represents a deep attractive well with an energy drop of $\sim 40 \text{ kcal/mol}$ from $R=12$ to 4 \AA . This efficient screening of the direct Coulomb interaction does not seem very surprising considering the high dielectric constant ($\epsilon_0=37.3$) of acetonitrile solvent: the IP curve may be comprehended as a screened Coulomb (plus steric repulsion at small R). Solvent caged minima in the mf potential curves are usually observed for "small" ions (like Na^+ , Cl^- , etc.) in polar solvents. It seems that the effect is smeared out for the larger polyatomic system studied here.

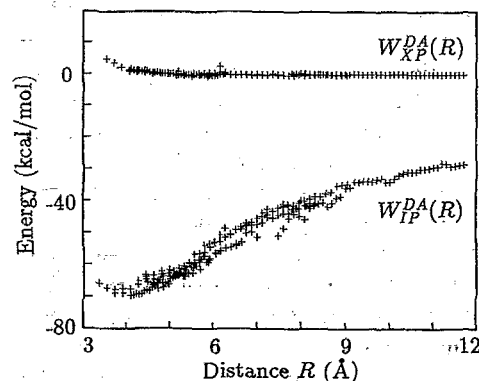


FIG. 4. Direct interaction components between DMA and anthracene $W_{\text{XP}}^{\text{DA}}(R)$ and $W_{\text{IP}}^{\text{DA}}(R)$ as a function of the DMA-anthracene center of mass distance R .

The encounter dynamics of the donor–acceptor pair may be viewed as a diffusion process on the mf potential. We compute the time-dependent mean square displacements defined by

$$d_i(\tau) = \langle |\mathbf{r}_i(t+\tau) - \mathbf{r}_i(t)|^2 \rangle \quad (i=D, A, \text{ and } DA), \quad (4.5)$$

where \mathbf{r}_D and \mathbf{r}_A denote the position of the c.m. of DMA and anthracene, respectively, and $\mathbf{r}_{DA} = \mathbf{r}_D - \mathbf{r}_A$. We found that $d_D(\tau)$ and $d_A(\tau)$ increase monotonically and almost linearly by time in both the XP and IP states, which reflects diffusive nature of their individual translational motion. In contrast, $d_{DA}(\tau)$ was found to deviate gradually from $d_D(\tau) + d_A(\tau)$ by time, which shows the correlation between \mathbf{r}_D and \mathbf{r}_A . The diffusion coefficient computed from the simulation results of $d(\tau)$ by

$$D_i = \lim_{\tau \rightarrow \infty} d_i(\tau)/6\tau \quad (i=D, A, \text{ and } DA) \quad (4.6)$$

are $D_D = 3.97 \times 10^{-5}$, $D_A = 3.17 \times 10^{-5}$, and $D_{DA} = 6.02 \times 10^{-5} \text{ cm}^2 \text{ s}^{-1}$ for XP states and $D_D = 1.83 \times 10^{-5}$, $D_A = 1.90 \times 10^{-5}$, and $D_{DA} = 3.06 \times 10^{-5} \text{ cm}^2 \text{ s}^{-1}$ for IP states, respectively. The Stokes–Einstein (SE) low,⁵⁷

$$D_{SE} = k_B T / n \pi \eta a \quad (n=4 \text{ or } 6), \quad (4.7)$$

with a (typical) solute radius $a = 4 \text{ \AA}$ (see Sec. IV C), the experimental solvent viscosity $\eta = 0.345 \text{ cP}$, the temperature $T = 298 \text{ K}$, and $n = 4$ gives $D_{SE} = 2.37 \times 10^{-5} \text{ cm}^2 \text{ s}^{-1}$.

C. Free energy relation

In Sec. II, we defined the solvation coordinate s which represents the stochastic one-dimensional dynamics of the solution phase reaction. Here the diabatic free energy curves along s are computed at several values of R and their dependence on R is studied. The computational method is as follows.⁴¹ The equilibrium MD simulations are carried out with the potential

$$W_{IP} + \alpha(W_{XP} - W_{IP}) \quad (4.8)$$

with the donor–acceptor distance R fixed. For $\alpha = 0$ and 1, the system evolves on the diabatic surfaces W_{IP} and W_{XP} , respectively. The free energy perturbation method with $0 < \alpha < 1$ is employed to interpolate thermally improbable regions of the free energy curves. The free energy curve $F(s; \alpha)$ for the coordinate s is defined by

$$F(s; \alpha) - F(s; 0) = -k_B T \ln \{ Q(s; \alpha) / Q(s; 0) \}, \quad (4.9)$$

where $Q(s; \alpha)$ denotes the partition function

$$Q(s; \alpha) \propto \int \delta[s - f(\mathbf{x})] \exp(-\beta \{ W_{IP}(\mathbf{x}) + \alpha [W_{XP}(\mathbf{x}) - W_{IP}(\mathbf{x})] \}) d\mathbf{x}, \quad (4.10)$$

which is related to the probability distribution of s directly computed from the simulation. From Eqs. (4.8)–(4.10) the following simple relation is derived:

$$F(s; \alpha) - F(s; 0) = \alpha s. \quad (4.11)$$

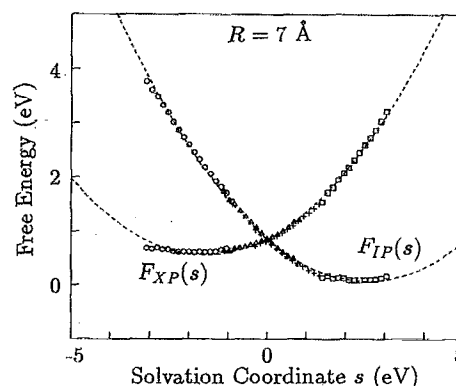


FIG. 5. Diabatic free energy curves along the solvation coordinate s . The distance between the center of mass of DMA and anthracene center is fixed at $R = 7 \text{ \AA}$. The symbols \square , Δ , \circ , and \times correspond to the equilibrium simulations with the parameter $\alpha = 0, 0.5, 0.7$, and 1.0 , respectively. Dashed curves are the least-squares fitted parabolas with a common value of the force constant for the two curves: $F_{XP}(s)$ and $F_{IP}(s)$.

The free energy curves are computed at $R = 5, 7, 9$, and 12 \AA from the equilibrium simulations of 75 ps for each. The result for $R = 7 \text{ \AA}$ is presented in Fig. 5. The curves are least-squares fitted to the form

$$F_{XP}(s) = \frac{K}{2} (s - s_0)^2, \quad F_{IP}(s) = F_{XP}(s) - s, \quad (4.12)$$

and the fitted parabolas are included in Fig. 5. An important consequence of Eq. (4.11) is that the force constants of $F_{XP}(s)$ and $F_{IP}(s)$ must be the same if the curves are exactly parabolic.⁵⁸ As seen in the figure, the free energy curves are well approximated by parabolas. All the other curves for $R = 5, 9$, and 12 \AA are also found to be well fitted by parabolas. These indicate that the nonlinear effects termed the “dielectric saturation”³⁴ have no significance in this reaction class.

The computed values of the free energy gap ΔG^0 , the activation energy ΔG^\ddagger , and the reorganization energy λ are summarized in Table III. ΔG^0 is nearly independent of R , which is also seen in the mf potential curves in Fig. 3. λ naturally becomes smaller as the donor–acceptor pair approaches. Figure 6 compares the simulation results of λ and the dielectric continuum Marcus model¹¹

TABLE III. Free energy relationships.

R^a	5	7	9	12
K^b	0.294	0.242	0.185	0.151
s_0	-1.13	-1.58	-2.26	-2.80
ΔG^0	-0.57	-0.49	-0.45	-0.52
λ	1.70 (0.79) ^c	2.07 (1.59)	2.71 (2.04)	3.32 (2.43)
ΔG^\ddagger	0.19 (0.02)	0.30 (0.17)	0.47 (0.28)	0.59 (0.37)

^a R is given in \AA .

^bThe force constant K is given in eV^{-1} .

^cEnergies are given in eV.

^dThe simulation uncertainties estimated are $\pm 0.06 \text{ eV}$ for s_0 , ΔG^0 , and λ .

^eThe values in parentheses are from the dielectric continuum model.

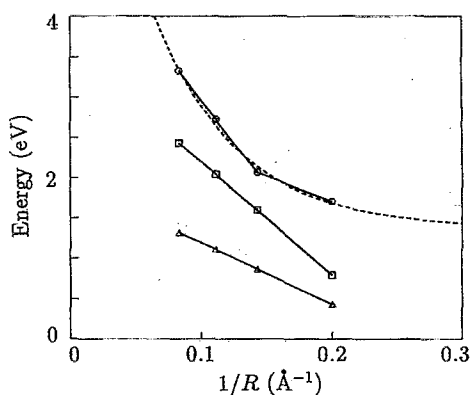


FIG. 6. Dependence of the reorganization energy λ on the inverse of the DMA-anthracene center of mass distance $1/R$. The symbols \circ , \square , and \triangle represent the simulation results, the dielectric continuum model with $\epsilon_\infty=1$ and 1.8, respectively. The dashed curve is a least-squares fitted one in the form [Eq. (4.15)].

$$\lambda(R) = (\Delta e)^2 \left(\frac{1}{\epsilon_\infty} - \frac{1}{\epsilon_0} \right) \left(\frac{1}{2a_D} + \frac{1}{2a_A} - \frac{1}{R} \right), \quad (4.13)$$

as a function of $1/R$. a_D and a_A are the effective radii of donor and acceptor molecules immersed in the dielectric continuum solvent. The experimental values of the static and optical dielectric constants⁵ ($\epsilon_0=37.3$, $\epsilon_\infty=1.8$) are used. A dielectric continuum plot with $\epsilon_\infty=1$ is also included in the figure for comparison, considering the simulation does not account for the solvent electronic polarization explicitly (though it is supposed to be included to some extent effectively by assigning a larger dipole moment of the solvent molecules than its gas-phase value).⁵⁹ The effective radii of DMA and anthracene used in Eq. (4.13) are estimated by using the intermolecular potential functions developed in Sec. III: the repulsive exchange-exclusion parts of the interaction potential curves are computed for 26 directions of approach, and the obtained length parameters are averaged with the weight of the numerical integration on a surface of sphere.^{41,56} The resultant radii are $a_D=4$ Å and $a_A=4$ Å.

We can see in Fig. 6 that the slope of the $\lambda-1/R$ plot from the simulation data is roughly reproduced by Eq. (4.13).⁶⁰ The quantitative difference between the simulation results and Eq. (4.13) is as large as 1 eV. It is noted that the absolute value of λ from Eq. (4.13) is sensitive to the estimate of the molecular radii. Similar values to the present simulation results could be obtained by applying a rather unrealistic molecular radii of $a_D=a_A=2.2$ Å,⁶¹ which shifts the dielectric continuum plot in Fig. 6 keeping its slope.

Reflecting the deviation seen in λ , the activation energy ΔG^\ddagger shows a significant difference between the simulation results and the dielectric continuum prediction (Table III). The simulation results of ΔG^\ddagger are always larger than the dielectric continuum predictions by about 0.1–0.2 eV. The dielectric continuum prediction of ΔG^\ddagger at $R=5$ Å is quite small which might be the basis for the statement that the present reaction with $\Delta G^0=-0.54$ eV corresponds to the region near inversion.²⁹ According to the simulation results, however, ΔG^0 of this reaction has not entered the inverted

region but corresponds to the increasing region of the rate $-\Delta G^0 < \lambda$. It would be worth pointing out, as well as the sensitivity to the molecular radii, that the arguments on the absence of the inverted region seem to have been based on a fitting of the experimental data of the increasing region to an inverted parabola without reasonable estimate of the reorganization energy.

The diabatic free energy surfaces $F(R,s)$ as a function of R and s are constructed by combining the above results. Because of the following two relations among $\lambda(R)$, $K(R)$, $s_0(R)$, and $\Delta G^0(R)$:

$$K(R) = 1/2\lambda(R), \quad s_0(R) = -\Delta G^0(R) - \lambda(R), \quad (4.14)$$

two variables are needed to construct $F(R,s)$. First, $\lambda(R)$ is least-squares fitted to a form,

$$\lambda(R) = r_1 \exp(-r_2/R) + r_3, \quad (4.15)$$

with $r_1=7.34$ eV, $r_2=15.8$ Å, and $r_3=1.37$ eV (the dotted curve in Fig. 6). $F_{XP}(R)$ and $F_{IP}(R)$ are represented in a form,

$$F(R) = c_1 \left\{ \left(\frac{c_2}{R} \right)^{2n} - \left(\frac{c_2}{R} \right)^n \right\} + c_3. \quad (4.16)$$

The least-squares optimized parameters are $c_1=2.06$ (3.69) kcal/mol, $c_2=4.98$ (4.31) Å, and $n=3.11$ (2.82) for the XP (IP) state. c_3 for the XP state is set to be zero and that for the IP state is determined so that $\Delta G^0(R)$ at $R=12$ Å reproduces the value in Table III. We used $F_{IP}(R) - F_{XP}(R)$ in place of $\Delta G^0(R)$, which has been checked to be consistent with the values in Table III within the simulation uncertainties. The fitted curves are shown in Fig. 3. Finally, the free energy surfaces are expressed by

$$F_{XP}(R,s) = F_{XP}(R) + \frac{1}{4\lambda(R)} [s + \lambda(R) + \Delta G^0(R)]^2, \quad (4.17a)$$

$$F_{IP}(R,s) = F_{XP}(R) - s. \quad (4.17b)$$

The lower surfaces are displayed in Fig. 7. The crossing seam at $s=0$, $F(R,0)$, is included in Fig. 3.

V. MECHANISM OF ET

A. Electronic coupling

The electronic coupling between the initial (ψ_{XP}) and the final (ψ_{IP}) diabatic states are evaluated with the use of the MOs of the reacting species. We use charge-localized diabatic states,

$$\psi_{XP} = \{ \mathcal{A}_1(\varphi_D^0 \varphi_A^*) - \mathcal{A}_2(\varphi_D^0 \varphi_A^*) \} / \sqrt{2}, \quad (5.1a)$$

$$\psi_{IP} = \{ \mathcal{A}_1(\varphi_D^+ \varphi_A^-) - \mathcal{A}_2(\varphi_D^+ \varphi_A^-) \} / \sqrt{2}, \quad (5.1b)$$

where $\varphi_D^0 \varphi_A^*$ and $\varphi_D^+ \varphi_A^-$ represent simple products of the MOs of DMA and anthracene for XP and IP states, respectively. \mathcal{A} denotes an antisymmetrizer, and \mathcal{A}_1 and \mathcal{A}_2 show different singlet couplings of the open shells. These diabatic states are nonorthogonal, $S_{XI} = \langle \psi_{XP} | \psi_{IP} \rangle \neq 0$, and the appropriate electronic coupling in terms of the symmetrically orthogonalized states is given by the matrix element⁶²

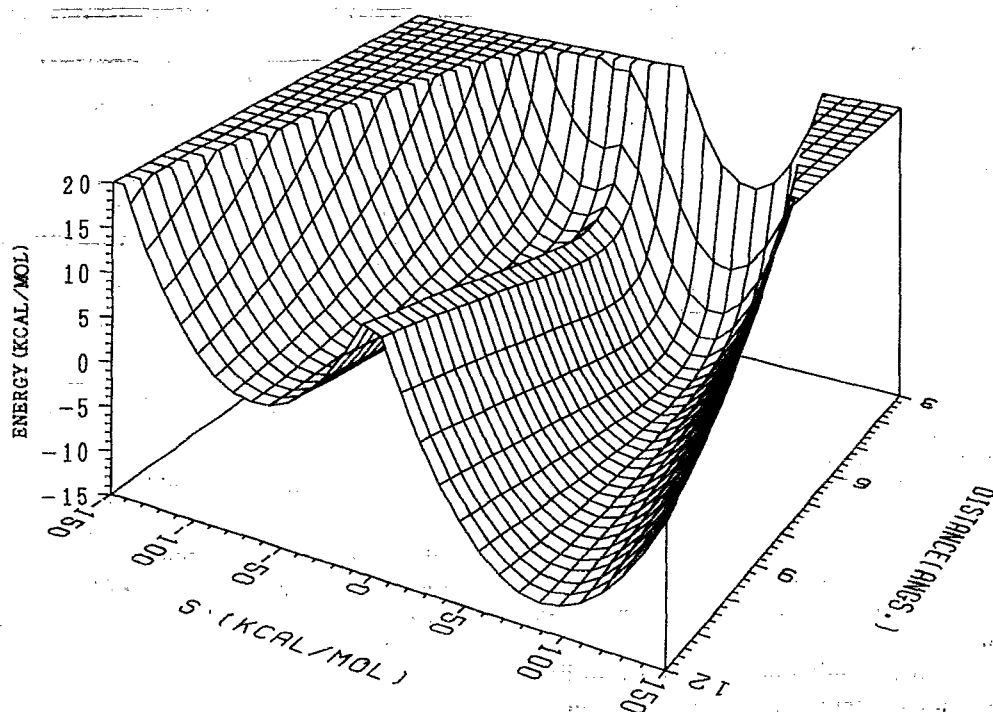


FIG. 7. Two-dimensional diabatic free energy surfaces $F_{XP,IP}(R,s)$ as a function of the DMA-anthracene center of mass distance R and the solvation coordinate s . Note that only the lower surfaces are shown.

$$H'_{XI} = \frac{H_{XI} - S_{XI}(H_{XX} + H_{II})/2}{1 - S_{XI}^2}, \quad (5.2)$$

where $H_{XI} = \langle \psi_{XP} | H_{el} | \psi_{IP} \rangle$ (and analogous for H_{XX} and H_{II}), and H_{el} is the electronic (Born–Oppenheimer) Hamiltonian. These values are computed at $R=5$ and 7 Å using the configurations sampled in the course of the MD simulation.

First, we evaluate the distribution of the overlap S_{XI} at the potential crossing $s=0$. The number of independently sampled configurations is 20 for each of $R=5$ and 7 Å. We use φ_D^0 , φ_D^+ , φ_A^* , and φ_A^- optimized in their isolated states (*in vacuo*). The mean and the variance of $|S_{XI}|$ computed are 4.18×10^{-3} and 4.01×10^{-3} for $R=5$ Å, and 2.84×10^{-3} and 1.81×10^{-3} for $R=7$ Å, respectively. The large variance comes from the relative orientational degrees of freedom between DMA and anthracene.

Next, a configuration that has the value of $|S_{XI}|$ closest to the mean value is picked up to compute H'_{XI} . Here, the MOs are recalculated under the influence of the electrostatic field from the effective point charges of the counter molecule and solvents: e.g., φ_D^0 is computed in the presence of the point charges of the excited state anthracene and about 250 acetonitrile molecules that are in a sphere with the radius $L/2$ centered at the c.m. of the DMA-anthracene pair.

The SCF calculations are carried out using the spin-restricted open-shell HF method. As discussed in Ref. 62, the electron correlation effects are expected to be canceled out to a large extent in the calculated H'_{XI} [see Eq. (5.2)]. The method of corresponding orbitals⁶³ is used for the computation of H'_{XI} because it involves sets of MOs which are not

mutually orthogonal. The basis function used is a 6-31G(N^*) set and the number of functions is 255 for the computation of H'_{XI} .⁶⁴

The values of $|S_{XI}|$ (without point charges) of the picked up configurations are 4.04×10^{-3} ($R=5$ Å) and 2.57×10^{-3} ($R=7$ Å). They changed to 5.44×10^{-3} and 3.26×10^{-3} with the existence of the point charges, respectively. $|H'_{XI}|$ is computed to be 1.92 and 0.84 kcal/mol for $R=5$ and 7 Å. Assuming an exponential form of the electronic coupling,

$$|H'_{XI}(R)|^2 = |H'_{XI}(R_0)|^2 \exp[-\gamma(R-R_0)], \quad (5.3)$$

with $R_0=5$ Å, $\gamma=0.83$ Å⁻¹ is obtained. This is used to evaluate the R -dependent rate constant $k(R)$.

B. ET rates from the nonadiabatic Golden Rule formula

Before projecting out the solvation coordinate from the bath modes as Eq. (2.10), the ET rate from the usual Golden Rule formalism is evaluated by using the (ω_i, \tilde{s}_i) data. The frequency components of the direction vector \tilde{s} are deduced from a spectral analysis of the velocity autocorrelation function of the solvation coordinate s , which are shown in Fig. 8 for $R=5$ and 7 Å. They are computed from the equilibrium trajectory on the potential $W_{IP} + \alpha(W_{XP} - W_{IP})$ with $\alpha=0.7$ to explore the region around the potential crossing. The components \tilde{s}_i are characterized by two main bands composed of several peaks with the maxima located at around 100 and

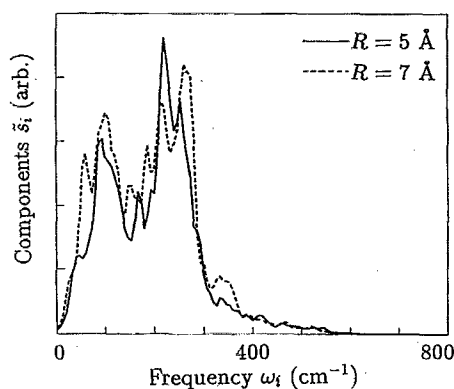


FIG. 8. Components of the reaction coordinate vector \tilde{s}_i^2 and frequencies ω_i . Solid and dashed curves correspond to the DMA-anthracene center of mass distance $R=5$ and 7 Å, respectively.

250 cm^{-1} . The former corresponds to the librational modes of the solvent acetonitrile and the latter mainly comes from the intramolecular modes of DMA.

With an assumption of equilibrium solvation with Boltzmann distribution with the temperature $\beta^{-1} = k_B T$, the nonadiabatic Golden Rule rate constant is given by^{22,23}

$$k_q = \frac{|H'_{XI}|^2}{\hbar^2} \int_0^\infty \exp[C(t)] dt, \quad (5.4a)$$

where

$$C(t) = \frac{4}{\pi \hbar} \int_0^\infty d\omega \frac{J(\omega)}{\omega^2} \left\{ [\cos \omega t - 1] \coth\left(\frac{\beta \hbar \omega}{2}\right) + i \sin \omega t \right\} + \frac{i \Delta G^0 t}{\hbar}, \quad (5.4b)$$

$$J(\omega) = \frac{\pi}{2} \sum_i \frac{c_i^2}{\omega_i} \delta(\omega - \omega_i), \quad (5.4c)$$

By using the sum relation

$$\frac{4}{\pi} \int_0^\infty d\omega \frac{J(\omega)}{\omega} = \lambda, \quad (5.5)$$

the last term in Eq. (5.4b) is included into the integral. The spectral density $J(\omega)$ is computed from the (ω_i, \tilde{s}_i) data, where Eq. (5.5) is used to scale the normalized \tilde{s}_i . Note that $J(\omega)$ in Eq. (5.4c) is different from $J_b(\omega)$ in Eq. (2.15). The evaluation of the integral is carried out by the stationary phase approximation¹⁵

$$k_q \approx \frac{|H'_{XI}|^2}{\hbar^2} \sqrt{\frac{2\pi}{|C''(t^*)|}} \exp[C(t^*)], \quad (5.6)$$

where t^* is the saddle point that gives $C'(t^*)=0$. t^* is given analytically for the symmetric reaction ($t^*=i\beta\hbar/2$) and for the one-dimensional case. As the present case is asymmetric and multidimensional with a general spectral density from the MD analysis, t^* is searched numerically on the pure imaginary axis by using the Newton-Raphson method.

The "semiclassical" form of the rate

TABLE IV. Nuclear tunneling effects.

R^a	5	7	9	12
k_{sc}/k_{cl}	1.097 (± 0.020)	1.136 (± 0.019)	1.224 (± 0.022)	1.290 (± 0.023)
k_q/k_{cl}	1.048 (± 0.006)	1.055 (± 0.004)	1.076 (± 0.003)	1.094 (± 0.003)
$t^*/i\beta\hbar$	0.331	0.381	0.417	0.421
$(1+\Delta G^0/\lambda)/2$	0.332	0.384	0.417	0.422

^a R is given in Å.

$$k_{sc} = \frac{|H'_{XI}|^2}{\hbar^2} \sqrt{\frac{2\pi}{A}} \exp\left\{-\frac{(\lambda + \Delta G^0)^2}{2\hbar^2 A}\right\}, \quad (5.7a)$$

$$A = \frac{4}{\pi \hbar} \int_0^\infty d\omega J(\omega) \coth\left(\frac{\beta \hbar \omega}{2}\right), \quad (5.7b)$$

is also derived by expanding $C(t)$ in powers of t and truncating at the second order (the short time approximation).^{32,35,38} Both k_q and k_{sc} reduce to the well-known form¹¹⁻¹⁵

$$k_{cl} = \frac{|H'_{XI}|^2}{\hbar} \sqrt{\frac{\pi}{\lambda k_B T}} \exp\left\{-\frac{(\lambda + \Delta G^0)^2}{4\lambda k_B T}\right\} \quad (5.8)$$

for small $\beta\hbar$.

The ratios k_q/k_{cl} and k_{sc}/k_{cl} which represent the quantum nuclear tunneling effects are computed and listed in Table IV. The saddle point t^* for k_q is also included in the table. It is seen that k_{sc}/k_{cl} is always larger than k_q/k_{cl} . As discussed in the literature,^{32,35,38} the semiclassical approximation generally overestimates (underestimates) the nuclear tunneling effect in the normal (inverted) region. The tunneling effects increase as R becomes larger, as the barrier at the diabatic crossing becomes more cuspidate. The solvent nuclear tunneling effects are no larger than 1.1 for the present system at the room temperature, which reflects the relatively low frequencies of the related modes (Fig. 8). Much larger effects have been found in the case of aqueous solutions^{38(b)} where the typical frequency of the librational solvent motion is as large as 800 cm^{-1} . It should be noted that the rate formula above is adequate in the nonadiabatic regime, i.e., the small electronic coupling limit. As discussed below, the electronic coupling estimated for the present specific system cannot be considered as small for $R < 7$ Å that the electronically adiabatic regime becomes more appropriate. The inclusion of the electronic coupling to construct the adiabatic surfaces would make the solvent nuclear tunneling effects even smaller, due to the resulting decrease of the effective barrier frequency.

It is also found that the computed values of $t^*/i\beta\hbar$ agree well with $|s_0|/(|s_0|+|s_1|) = (1+\Delta G^0/\lambda)/2$ where s_0 and s_1 are the minima of the free energy curves $F_{XP}(s)$ and $F_{IP}(s)$. This simple relation shows an interesting connection to the path integral interpretation of the saddle point imaginary time-correlation function (TCF) in the Golden Rule rate formula²⁵: the isomorphism between the saddle point TCF and the equilibrium partition function of a "polymer chain" in a discretized path integral representation. In fact, the agreement found here stands only approximately, i.e.,

$t^*/i\beta\hbar$ is not exactly linear in ΔG^0 , and this approximation depends on the characteristic frequency range of the spectral density $J(\omega)$. More detailed and general aspects of this issue will be pursued elsewhere.

C. ET rate and mechanism as functions of the donor–acceptor distance

The outer-sphere ET reactions have usually been considered in the nonadiabatic regime as in the above section. However, the electronic coupling of the present system becomes as large as 2 kcal/mol at $R=5$ Å, and the reaction mechanism should be adequately described by the (electronically) adiabatic regime as R becomes smaller.⁶⁵ We consider an interpolation formula between the adiabatic and the nonadiabatic regimes:

$$k = \frac{2P_{LZ}\kappa_{ad}}{\kappa_{ad} + P_{LZ}(2 - \kappa_{ad})} k^{TST}, \quad (5.9a)$$

$$k^{TST} = \frac{\Omega}{2\pi} \exp(-\Delta G_{ad}^\ddagger/k_B T), \quad (5.9b)$$

where P_{LZ} and κ_{ad} are the Landau–Zener transition probability^{7,24–28} and an adiabatic transmission coefficient, respectively. The prefactor in Eq. (5.9a) was derived by Straub and Berne²⁷ by assuming the crossings are independent and thus neglecting the quantum interference.²⁴ A similar form has also been derived by Spargaglione and Mukamel.⁶⁶ Equation (5.9a) reduces to a semiclassical Landau–Zener form, $2P_{LZ}/(1+P_{LZ})k^{TST}$, for the $\kappa_{ad} \rightarrow 1$ limit, and to an adiabatic form, $\kappa_{ad}k^{TST}$, for $P_{LZ} \rightarrow 1$ (or the large electronic coupling limit). The velocity at the crossing is represented by its thermal average, i.e., $P_{LZ} \approx 1 - \exp(-2\pi|H'_{XI}|^2/\hbar\sqrt{\langle\dot{s}^2\rangle})$. The mean square velocity $\langle\dot{s}^2\rangle$ is related to the effective mass μ by $\mu = k_B T/\langle\dot{s}^2\rangle$, which leads to a more useful form:

$$P_{LZ}(R) = 1 - \exp\left(-\frac{\sqrt{2}\pi}{\hbar\Omega} \frac{|H'_{XI}(R)|^2}{\sqrt{k_B T\lambda(R)}}\right). \quad (5.10)$$

The barrier frequency ω_b is evaluated as follows. First, the adiabatic (lower) free energy curve is expressed by the diabatic $F_{XP,IP}(s;R)$,

$$E(s;R) = \frac{1}{2}[F_{XP}(s) + F_{IP}(s)] - \frac{1}{2}[(F_{XP}(s) - F_{IP}(s))^2 + 4|H'_{XI}|^2]^{1/2}, \quad (5.11)$$

where the parametrical dependence on R is abbreviated on the right-hand side of the equation. The square of ω_b is evaluated from the curvature at the barrier top $s_\ddagger(R)$ that gives $\partial E/\partial s|_{s=s_\ddagger} = 0$,

$$\begin{aligned} \omega_b(R)^2 &= -\frac{1}{\mu} \frac{\partial^2 E}{\partial s^2} \bigg|_{s=s_\ddagger} \\ &= \Omega^2 \left[\frac{\lambda}{\sqrt{s_\ddagger^2 + 4|H'_{XI}|^2}} \left\{ 1 - \frac{s_\ddagger^2}{s_\ddagger^2 + 4|H'_{XI}|^2} \right\} - 1 \right]. \end{aligned} \quad (5.12)$$

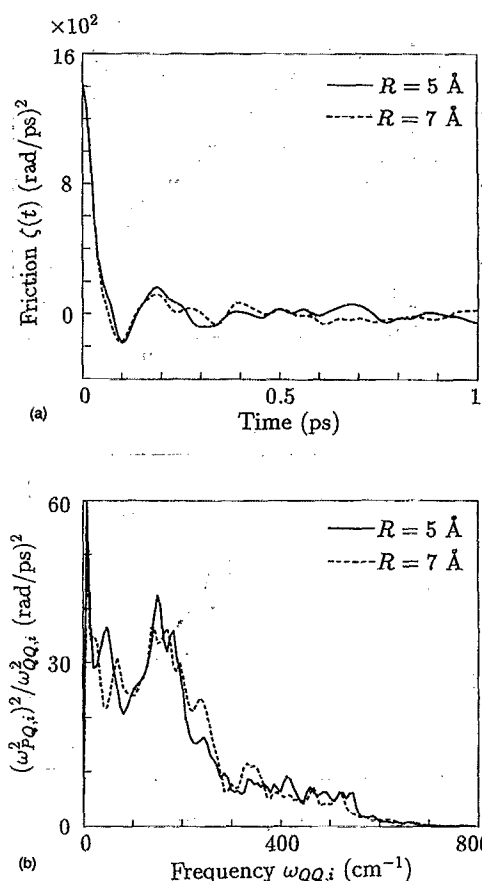


FIG. 9. (a) Time-dependent friction kernel $\zeta(t)$. (b) Frequency components of the friction kernel, i.e., $(\tilde{\omega}_{PQ,i}^2)/\tilde{\omega}_{QQ,i}^2$ as a function of $\tilde{\omega}_{QQ,i}$. Solid and dashed curves correspond to the DMA-anthracene center of mass distance $R=5$ and 7 Å, respectively.

Several choices would be possible for κ_{ad} . Here we employ the Grote–Hynes transmission coefficient κ_{GH} , which is computed by⁶⁷

$$\kappa_{GH} = z_r/\omega_b, \quad z_r^2 + z_r\hat{\zeta}(z_r) - \omega_b^2 = 0, \quad (5.13a)$$

where $\hat{\zeta}(z)$ is the Laplace transform of $\zeta(t)$,

$$\hat{\zeta}(z) = \sum_i \frac{(\tilde{\omega}_{PQ,i}^2)}{\tilde{\omega}_{QQ,i}^2} \frac{z}{z^2 + \tilde{\omega}_{QQ,i}^2}. \quad (5.13b)$$

All these dynamical quantities are deduced from the MD trajectory analysis by the procedure described in Sec. II. The computed values for $R=5$ (7) Å are summarized as follows: the characteristic frequency $\tilde{\omega} = (\sum_i \tilde{s}_i^2 \omega_i^2)^{1/2} = 219$ (215) cm^{-1} , the effective frequency $\Omega = [\tilde{\omega}^2 - \zeta(0)]^{1/2} = 92$ (86) cm^{-1} , and the effective mass $\mu = k_B T/\langle\dot{s}^2\rangle = 0.95 \times 10^{-3}$ (0.71×10^{-3}) $\text{ps}^2 \text{eV}^{-1}$. The effective frequency by the Gaussian approximation $\Omega' = (\langle\dot{s}^2\rangle/\langle\dot{s}^2\rangle)^{1/2}$ is computed to be 88 (85) cm^{-1} . The effective frequency is also evaluated by $\Omega'' = \sqrt{K/\mu}$ which gives 93 (98) cm^{-1} . The degree of the coincidence among Ω , Ω' , and Ω'' would be a measure of the adequacy of the harmonic bath model.

Figure 9 displays the time-dependent friction kernel $\zeta(t)$ and the plot of its frequency component

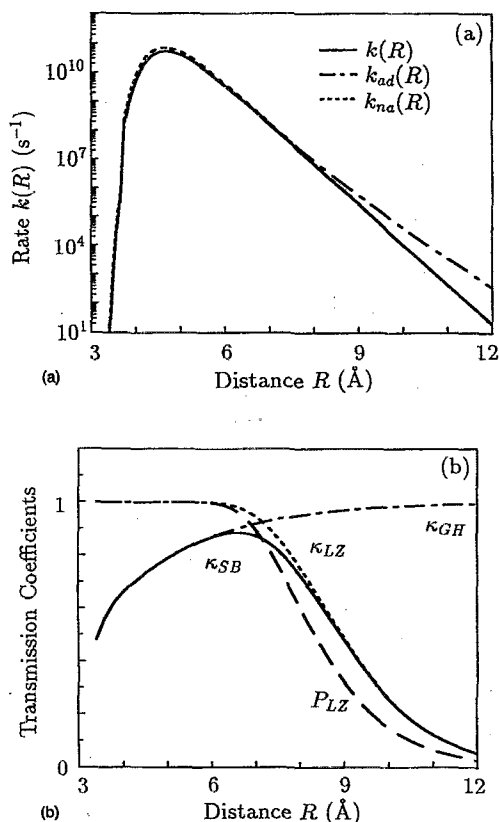


FIG. 10. (a) ET rates $k(R)$ [—], $k_{ad}(R)$ [---], and $k_{na}(R)$ [· · ·] as functions of the DMA-anthracene center of mass distance R . (b) Transmission coefficients $\kappa_{SB}(R)$ [—], $\kappa_{GH}(R)$ [---], and $\kappa_{LZ}(R)$ [· · ·]. The Landau-Zener transition probability $P_{LZ}(R)$ [— · —] is also included.

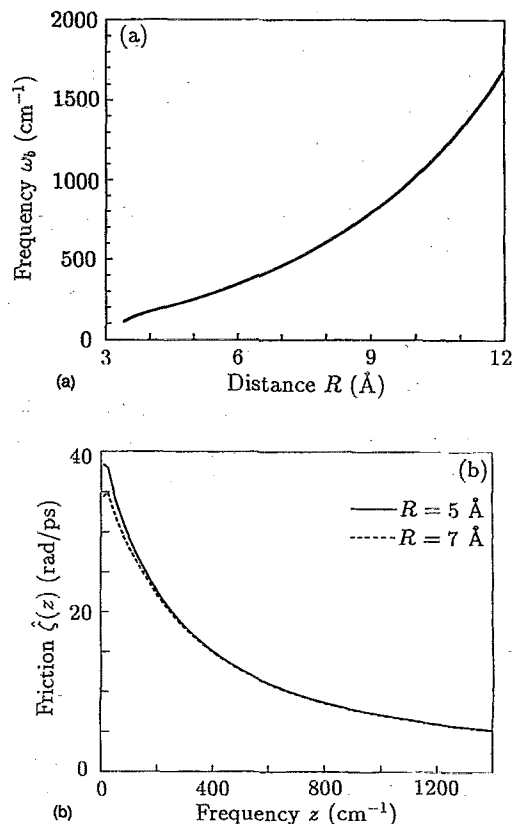


FIG. 11. (a) The barrier frequency $\omega_b(R)$ as a function of the DMA-anthracene center of mass distance R . (b) The Laplace transform of the friction kernel $\hat{\zeta}(z)$. z is given in cm $^{-1}$ (i.e., $z/2\pi$).

$[\tilde{\omega}_{QO,i}, (\tilde{\omega}_{PQ,i}^2/\tilde{\omega}_{QO,i}^2)]$, which is related to the spectral density $J_b(\omega)$. As seen in the figure, $\zeta(t)$ shows a rapid decay within ~ 0.1 ps, descends down to negative values, and accompanies a small oscillation with an interval of ~ 0.2 ps. The rapid decay of $\zeta(t)$ is reflected in the overdamped behavior of the relaxation of s .

The R -dependent rate $k(R)$ is computed and displayed in Fig. 10(a). The activation energy $\Delta G_{ad}^\ddagger(R)$ is computed from the adiabatic curve $E(s;R)$. We assume that Ω is independent of R and uses a constant value of 90 cm $^{-1}$. For comparison, the adiabatic and the nonadiabatic limits $k_{ad} = \kappa_{GH} k^{\text{TST}}$ and $k_{na} = 2P_{LZ}/(1+P_{LZ}) k^{\text{TST}}$ are included in the figure. The R dependence of the transmission coefficients κ_{GH} , $\kappa_{na} = 2P_{LZ}/(1+P_{LZ})$, and $\kappa_{SB} = 2P_{LZ}\kappa_{GH}/[\kappa_{GH} + P_{LZ}(2 - \kappa_{GH})]$ are also shown in Fig. 10(b). We can see in the figure that the ET mechanism switches from nonadiabatic to adiabatic as R becomes smaller. The R dependence of the rate $k(R)$ is primarily determined by the activation energy [see also $F(R,0)$ in Fig. 3] and the maximum of $k(R)$ is located at around $R=5$ Å.

In Fig. 11, ω_b and $\hat{\zeta}(z)$ are shown. The barrier frequency $\omega_b(R)$ increases nearly exponentially by R , and becomes as large as 1700 cm $^{-1}$ at $R=12$ Å. As the relevant frequency increases, $\hat{\zeta}(z)$ decreases rapidly and consequently the Grote-Hynes transmission coefficient κ_{GH} approaches unity.

VI. CONCLUDING REMARKS

In this work, we carried out a theoretical analysis on the photoinduced intermolecular ET reaction between DMA and anthracene in acetonitrile solution, on the basis of realistic molecular modelings—*ab initio* MO calculations of the potential energy surfaces and MD simulations of the solution phase reaction. Considering the ET may occur over a range of the donor-acceptor distance R , mean force potential curves along R and the encounter dynamics on them in solution were investigated. It was found that the encounter dynamics is viewed as a diffusion process on a rather flat mean force potential, even for the ion pair state.

Free energy curves along the solvation coordinate s were computed and found to be well approximated by parabolas, indicating that the nonlinear effects such as the dielectric saturation are negligibly small. The free energy surfaces as a function of R and s were constructed to examine the free energy relationships. It was pointed out that the present system with the energy gap $\Delta G^0 = -0.54$ eV corresponds to the increasing region of the rate constant in acetonitrile solution, in contrast with the conventional picture.

The electronic coupling of the ET was evaluated by the method of corresponding orbitals. The ET rate was computed as a function of R , with the use of a simple interpolation formula between the adiabatic and the (semiclassical) nonadiabatic regimes. It was shown that the ET mechanism is

primarily described by the nonadiabatic regime in $R > 8 \text{ \AA}$ and by the adiabatic regime in $R < 6 \text{ \AA}$. The dynamical solvent friction effects were taken into account in terms of the generalized Langevin equation formalism.

The present study is on a specific system of DMA and anthracene in acetonitrile solution. In the experimental study by Rehm and Weller,²⁹ the fluorescence quenching ET rates have been measured as a function of ΔG^0 in acetonitrile solution, and the inverted behavior was not observed down to ΔG^0 of about -2.5 eV . According to the present study, the maximum of the rate constant in acetonitrile solution should be found around $\Delta G^0 = -\lambda \approx -1.7 \text{ eV}$, considering the energetics obtained here for $R = 5 \text{ \AA}$ [where the maximum of $k(R)$ is located] and assuming that the major part of the reorganization comes from the solvent and is almost independent of the solute species. It is noted that the inverted behavior is observed for the charge recombination ET reactions in acetonitrile solution by the picosecond time-resolved transient absorption spectroscopy.⁶⁸ The maximum of the rate ΔG^0 plot is located at around $\Delta G^0 \approx -1.6 \text{ eV}$, which is consistent with the present results. The present results seem to support the following interpretation^{31,32} of the experimentally observed plateau region of the CS rate: *the activation rates k_{act} around $\Delta G^0 = -1.7 \text{ eV}$ are large enough that the observed rates k_{obs} by the steady-state measurements are masked by diffusion*. In the present case, $k(R)$ has a sharp peak located at $R_0 \approx 5 \text{ \AA}$ [see the log scale of the ordinate in Fig. 10(a)]. In such a case,^{10,32} the diffusion controlled rate k_{diff} is well described by $k_{diff} \approx 4\pi D_{DA} R_0$ and k_{obs} is given by $k_{obs}^{-1} \approx k_{diff}^{-1} + k_{act}^{-1}$. The computed value of k_{diff} for the present system is $2.28 \times 10^{10} \text{ M}^{-1} \text{ s}^{-1}$, using $D_{DA} = 6.02 \times 10^{-5} \text{ cm}^2 \text{ s}^{-1}$ and $R_0 = 5 \text{ \AA}$, which is in reasonable agreement with the experimentally observed plateau region of the CS rate. It is rather difficult to compare the calculated k_{act} with the experimental results because of its sensitivity to the activation energy. We computed k_{act} by

$$k_{act} = 4\pi \int_{R_1}^{\infty} k(R) R^2 dR, \quad (6.1)$$

in which R_1 denotes a contact distance (taken to be 3.5 \AA), and obtained $k_{act} = 9.51 \times 10^9 \text{ M}^{-1} \text{ s}^{-1}$. Although key quantities such as the electronic coupling should differ in each system, k_{act} could be estimated to be about 10^2 times larger at the inversion maximum $\Delta G^0 = -\lambda$, which gives k_{obs} masked by diffusion, $k_{obs} \approx k_{diff}$. The actual difference of the electronic coupling among the different fluorescer-quencher pairs used in the experiment can be regarded as small that it would not alter the essential argument.

More extensive studies would be needed for a satisfactory understanding of the ET mechanisms. As noted above, key quantities that determine the rate should be evaluated on each specific system in order to make a reliable comparison with the experiment. More accurate intra- and intermolecular potentials and larger simulations would be required to achieve quantitative results.

We employed a rather simple rate formula in Sec. V, which has an advantage of a clearly understandable picture. The neglect of the quantum interference leads to a simple interpolation formula, which would be a reasonable approxi-

mation since the interference effects are normally smeared out in multidimensional thermal rate constants at moderately high temperatures.²⁴ However, more precise theoretical developments are of importance which would be directed towards, e.g., (1) environmental effects on the electronic coupling—tunneling path,⁶⁹ renormalization by the solvent fluctuations,⁷⁰ etc.; (2) nonequilibrium effects of the solvation—competition between the electronic transition and the environmental relaxation;⁷¹ and (3) general quantum rate theories which consistently cover both the nonadiabatic and adiabatic regimes^{23,66,72} keeping usefulness for practical applications.

We hope to report studies on these issues based on realistic molecular modelings in the future.

ACKNOWLEDGMENTS

This work was supported by a Fellowship of the Japan Society for the Promotion of Science and the Grants in Aid for Scientific Research from the Ministry of Education associated with the Fellowship. Numerical calculations were carried out at the IMS Computer Center and Data Processing Center of Kyoto University. The author is grateful to Professor Shigeki Kato for his interest and useful comments.

- ¹ H. Beens and A. Weller, in *Organic Molecular Photophysics*, edited by J. B. Birks (Wiley Interscience, London, 1975), Vol. 2, p. 159.
- ² E. M. Kosower and D. Huppert, *Annu. Rev. Phys. Chem.* **37**, 127 (1986).
- ³ P. F. Barbara and W. Jarzeba, *Acc. Chem. Res.* **21**, 195 (1988); *Adv. Photochem.* **15**, 1 (1990).
- ⁴ G. E. McManis and M. J. Weaver, *Acc. Chem. Res.* **23**, 294 (1990).
- ⁵ M. Maroncelli, J. McInnis, and G. R. Fleming, *Science* **243**, 1674 (1989).
- ⁶ G. R. Fleming and P. G. Wolynes, *Physics Today* **43**, 36 (1990).
- ⁷ H. Frauenfelder and P. G. Wolynes, *Science* **229**, 337 (1985).
- ⁸ R. A. Marcus and N. Sutin, *Biochim. Biophys. Acta* **811**, 265 (1985).
- ⁹ M. D. Newton and M. Sutin, *Annu. Rev. Phys. Chem.* **35**, 437 (1984).
- ¹⁰ J. T. Hynes, in *The Theory of Chemical Reaction Dynamics*, edited by M. Baer (Chemical, Rubber Boca Raton, FL, 1985), Vol. 4, p. 171.
- ¹¹ R. A. Marcus, *J. Chem. Phys.* **24**, 966, 979 (1956); *Annu. Rev. Phys. Chem.* **15**, 155 (1964).
- ¹² V. G. Levich, *Adv. Electrochem. Electrochem. Eng.* **4**, 249 (1966).
- ¹³ R. R. Dogonadze and A. M. Kunznetsov, *Sov. Electrochem. Engl. Transl.* **3**, 1189 (1967).
- ¹⁴ J. J. Hopfield, *Proc. Natl. Acad. Sci. U.S.A.* **71**, 3640 (1974).
- ¹⁵ J. Ulstrup, *Charge Transfer Processes in Condensed Media* (Springer, Berlin, 1979).
- ¹⁶ J. T. Hynes, *J. Phys. Chem.* **90**, 3701 (1986).
- ¹⁷ R. I. Cukier, *J. Chem. Phys.* **88**, 5594 (1988).
- ¹⁸ L. D. Zusman, *Chem. Phys.* **49**, 295 (1980); **80**, 29 (1983).
- ¹⁹ D. F. Calef and P. G. Wolynes, *J. Phys. Chem.* **87**, 3387 (1983); *J. Chem. Phys.* **78**, 470 (1983).
- ²⁰ H. L. Friedman and M. D. Newton, *Discuss. Faraday Soc.* **74**, 73 (1982).
- ²¹ H. Sumi and R. A. Marcus, *J. Chem. Phys.* **84**, 4894 (1985).
- ²² A. J. Leggett, S. Chakravarty, A. Dorsey, M. P. A. Fisher, A. Garg, and W. Zwerger, *Rev. Mod. Phys.* **59**, 1 (1987), and references therein.
- ²³ A. Garg, J. N. Onuchic, and V. Ambegaokar, *J. Chem. Phys.* **83**, 4491 (1985).
- ²⁴ J. N. Onuchic and P. G. Wolynes, *J. Phys. Chem.* **92**, 6495 (1988).
- ²⁵ P. G. Wolynes, *J. Chem. Phys.* **87**, 6559 (1987).
- ²⁶ R. E. Cline, Jr. and P. G. Wolynes, *J. Chem. Phys.* **86**, 3836 (1987).
- ²⁷ J. E. Straub and B. J. Berne, *J. Chem. Phys.* **87**, 6111 (1987).
- ²⁸ D. P. Ali and W. H. Miller, *J. Chem. Phys.* **78**, 6640 (1983).
- ²⁹ D. Rehm and A. Weller, *Isr. J. Chem.* **8**, 259 (1970).
- ³⁰ (a) N. Mataga, Y. Kanda, T. Asahi, H. Miyasaka, T. Okada, and T. Kakitani, *Chem. Phys.* **127**, 239 (1988); (b) **127**, 249 (1988).
- ³¹ J. R. Miller, J. V. Beitz, and R. K. Huddleston, *J. Am. Chem. Soc.* **106**, 3047, 5057 (1984).
- ³² (a) P. Siders and R. A. Marcus, *J. Am. Chem. Soc.* **103**, 748 (1981); (b) R.

- A. Marcus and P. Siders, *J. Phys. Chem.* **86**, 622 (1982).
- ³³ S. Erima and M. Bixon, *J. Chem. Phys.* **64**, 3639 (1976).
- ³⁴ (a) T. Kakitani and N. Mataga, *J. Phys. Chem.* **89**, 4752 (1985); **90**, 993 (1986); **91**, 6277 (1987); (b) Y. Hatano, M. Saito, T. Kakitani, and N. Mataga, *ibid.* **92**, 1008 (1988).
- ³⁵ (a) J. K. Hwang and A. Warshel, *J. Am. Chem. Soc.* **109**, 715 (1987); (b) A. Warshel and J. K. Hwang, *J. Chem. Phys.* **84**, 4938 (1986); (c) G. King and A. Warshel, *ibid.* **93**, 8682 (1990).
- ³⁶ (a) E. A. Carter and J. T. Hynes, *J. Phys. Chem.* **93**, 2184 (1989); (b) J. Chem. Phys. **94**, 5961 (1991).
- ³⁷ D. A. Zichi, G. Ciccotti, J. T. Hynes, and M. Ferrario, *J. Phys. Chem.* **93**, 6262 (1989).
- ³⁸ (a) R. A. Kuharski, J. S. Bader, D. Chandler, M. Spirk, M. L. Klein, and R. W. Impey, *J. Chem. Phys.* **89**, 3248 (1988); (b) J. S. Bader, R. A. Kuharski, and D. Chandler, *ibid.* **93**, 230 (1990).
- ³⁹ (a) S. Kato, R. L. Jaffe, A. Komornicki, and K. Morokuma, *J. Chem. Phys.* **78**, 4567 (1983); (b) S. Kato, *ibid.* **88**, 3045 (1988).
- ⁴⁰ S. Kato and Y. Amatatsu, *J. Chem. Phys.* **92**, 7241 (1990).
- ⁴¹ K. Ando and S. Kato, *J. Chem. Phys.* **95**, 5966 (1991).
- ⁴² We used the program HONDO7 for the SCF calculations; M. Dupuis, J. D. Watts, H. O. Villar, and G. J. B. Hurst, HONDO Ver. 7.0, QCPE 544 (1987).
- ⁴³ E. R. Davidson, *Chem. Phys. Lett.* **21**, 565 (1973); C. F. Jackels and E. R. Davidson, *Int. J. Quantum Chem.* **7**, 707 (1974); F. W. Bobrowicz and W. A. Goddard III, in *Modern Theoretical Chemistry* (Plenum, New York, 1977).
- ⁴⁴ (a) A. Bree and S. Katagiri, *J. Mol. Spectrosc.* **17**, 24 (1965), and references therein; (b) D. P. Craig and P. C. Hobbins, *J. Chem. Soc.* **1955**, 2309; (c) J. Sidman, *J. Chem. Phys.* **25**, 115 (1956).
- ⁴⁵ J. H. Callomon, E. Hirota, K. Kuchitsu, W. J. Lafferty, A. G. Maki, C. S. Pote, I. Buck, and B. Starck, *Structure Data of Free Polyatomic Molecules* (Springer, Berlin, 1976).
- ⁴⁶ W. J. Hehre, R. Ditchfield, and J. A. Pople, *J. Chem. Phys.* **56**, 2252 (1972); (b) J. S. Binkley, J. A. Pople, and W. J. Hehre, *J. Am. Chem. Soc.* **102**, 939 (1980).
- ⁴⁷ W. R. Lambert, P. M. Felker, J. A. Syage, and A. H. Zewail, *J. Chem. Phys.* **81**, 2195 (1984).
- ⁴⁸ D. Biermann and W. Schmidt, *J. Am. Chem. Soc.* **102**, 3163 (1980).
- ⁴⁹ R. G. Gordon and Y. S. Kim, *J. Chem. Phys.* **56**, 3122 (1972).
- ⁵⁰ W. L. Jorgensen, J. D. Madura, and C. J. Swenson, *J. Am. Chem. Soc.* **106**, 6638 (1984).
- ⁵¹ W. L. Jorgensen and J. M. Briggs, *Mol. Phys.* **63**, 547 (1988).
- ⁵² D. J. Evans and S. Murad, *Mol. Phys.* **34**, 327 (1977).
- ⁵³ See the textbook M. P. Allen and D. J. Tildesley, *Computer Simulation of Liquids* (Clarendon, Oxford, 1987).
- ⁵⁴ C. W. Gear, *Numerical Initial Value Problems in Ordinary Differential Equations* (Prentice-Hall, Englewood Cliffs, NJ, 1971).
- ⁵⁵ D. J. Adams, E. H. Adams, and G. J. Hills, *Mol. Phys.* **38**, 387 (1979).
- ⁵⁶ M. Abramowitz and I. A. Stegun, *Handbook of Mathematical Functions* (Dover, New York, 1970).
- ⁵⁷ See, for example, J. T. Hynes, *Annu. Rev. Phys. Chem.* **28**, 301 (1977).
- ⁵⁸ M. Tachiya, *J. Phys. Chem.* **93**, 7050 (1989); A. Yoshimori, T. Kakitani, Y. Enomoto, and N. Mataga, *ibid.* **93**, 8316 (1989).
- ⁵⁹ On the solvent electronic polarization effects see, for example, H. J. Kim and J. T. Hynes, *J. Phys. Chem.* **96**, 5088 (1992); J. N. Gehlen, D. Chandler, J. J. Kim, and J. T. Hynes, *J. Phys. Chem.* **96**, 1748 (1992); R. A. Marcus, *ibid.* **96**, 1753 (1992).
- ⁶⁰ It is not adequate to apply Eq. (4.13) for $R < a_D + a_A$. The trend seen in the simulation results of Fig. 7 can possibly be better reproduced within the dielectric continuum model by taking account of the cavity overlap; B. J. Gertner and J. T. Hynes (private communication).
- ⁶¹ T. Kakitani, A. Yoshimori, and N. Mataga, *J. Phys. Chem.* **96**, 5385 (1992).
- ⁶² M. D. Newton, *Int. J. Quantum Chem. Symp.* **14**, 363 (1980); J. Logan and M. D. Newton, *J. Chem. Phys.* **78**, 4086 (1983).
- ⁶³ H. F. King, R. E. Stanton, H. Kim, R. E. Wyatt, and R. G. Parr, *J. Chem. Phys.* **47**, 1936 (1967).
- ⁶⁴ The code for the computation of H'_{kl} is written so as to make direct use of the two-electron integrals and not to require the disk storage.
- ⁶⁵ The electronic coupling obtained in Sec. V A is a "static" one, neglecting the possible renormalization of the coupling due to the solvent fluctuations. See Ref. 70, and references therein.
- ⁶⁶ M. Sparpagione and S. Mukamel, *J. Chem. Phys.* **88**, 3263 (1988).
- ⁶⁷ R. F. Grote and J. T. Hynes, *J. Chem. Phys.* **73**, 2715 (1980).
- ⁶⁸ S. Nishikawa, T. Asahi, T. Okada, N. Mataga, and T. Kakitani, *Chem. Phys. Lett.* **185**, 237 (1991).
- ⁶⁹ A. Kuki and P. G. Wolynes, *Science* **236**, 1647 (1987); C. A. Naleway, L. A. Curtiss, and J. R. Miller, *J. Phys. Chem.* **95**, 8434 (1991); J. N. Onuchic and D. N. Beratan, *J. Am. Chem. Soc.* **109**, 6771 (1987).
- ⁷⁰ B. Carmeli and D. Chandler, *J. Chem. Phys.* **82**, 3400 (1985); D. Chandler, *J. Stat. Phys.* **42**, 49 (1986).
- ⁷¹ N. Shima and M. Tsukada, *Surf. Sci.* **194**, 3121 (1988); M. Tsukada and Z. W. Gortel, *Phys. Rev. B* **38**, 3892 (1988).
- ⁷² J. N. Gehlen and D. Chandler, *J. Chem. Phys.* **97**, 4958 (1992); I. Rips and J. Jortner, *ibid.* **87**, 2090 (1987).